Quantum Inspire Starmon-5 Fact Sheet

(Dated: June 15, 2020)

This fact sheet provides further information on the Starmon-5 quantum processor, dilution refrigerator, control electronics, qubit operations and reported metrics.

I. QUANTUM PROCESSOR CHIP

Starmon-5 is a superconducting quantum processor based on circuit quantum electrodynamics [1, 2]. It consists of five transmon qubits [3] in an X-shaped coupling configuration. A schematic of the 8 mm×8 mm chip is shown in Fig. 1. Dedicated bus resonators connect nearest-neighbor pairs, enabling two-qubit gates. Each qubit is also connected to a microwave-control line for single-qubit gating, a flux-control line for two-qubit gating, and a dispersively-coupled resonator for readout. Every readout resonator has an accompanying Purcell filter [4]. The readout resonator structures for qubits Q_0, Q_2, Q_3, and Q_4 couple to one feedline, and those for qubit Q_1 to another. The unique frequencies of readout structures on a common feedline allow simultaneous, independent qubit readout by frequency multiplexing. The high-connectivity of these transmon qubits (up to 7 ports) gives them a characteristic star shape and hence the nickname *Starmon* [5]. All inputs and outputs to the chip are connected to a Cu printed circuit board using Al wirebonding, as shown in Fig. 2.

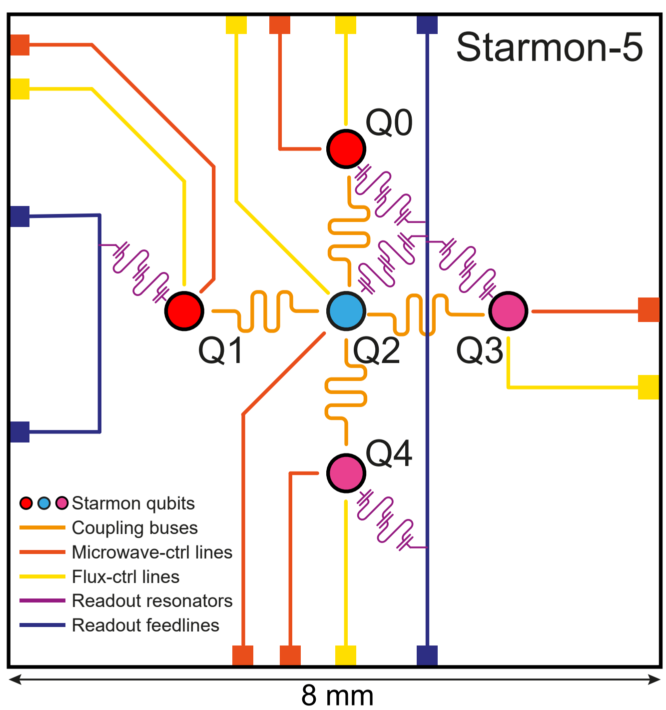

FIG. 1. Schematic diagram of the Starmon-5 quantum processor chip.

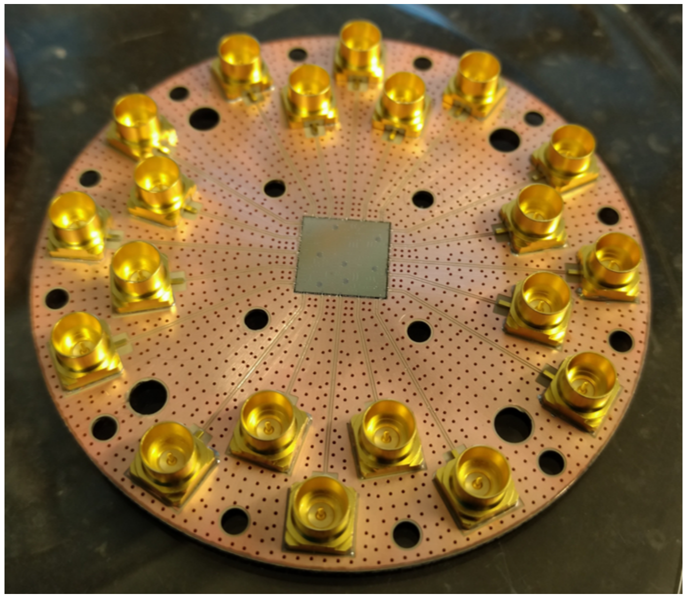

FIG. 2. Optical image of a similar device mounted onto the printed circuit board.

II. DILUTION REFRIGERATOR WIRING

Starmon-5 is cooled in a ^{3}He/^{4}He dilution refrigerator (Leiden Cryogenics CF-650) with a base temperature of 27 mK. A detailed diagram of the wiring of readout, microwave-control, and flux-control lines inside the refrigerator is shown in Fig. 3. The status of the refrigerator can be followed in real time via this link.

III. CONTROL ELECTRONICS

The Starmon-5 processor is controlled using a room-temperature electronics stack. This stack combines special-purpose QuTech-built and commercial electronics, as shown in the schematic in Fig. 4.

The QuTech Central Controller is an all-digital instrument whose primary function is to orchestrate the action of all control and readout instruments. This sequencer can generate up to 50 million sequences per instrument per second. It makes use of a distributed architecture to control up to 12 analog instruments per rack, ensuring the flexibility and extensibility of the control setup beyond Starmon-5. It achieves this while guaranteeing timing determinism.

The Zurich Instruments High-Density Arbitrary Waveform Generator is an eight-channel arbitrary waveform generator (AWG) which we use to produce both the flux pulses required for two-qubit gates and the envelopes of microwave pulses used for single-qubit gates. The HDAWG has real-time filtering capabilities that we use to correct the linear-dynamical distortions in the flux-control lines [6]. Starmon-5 makes use of 3 HDAWGs.

The Zurich Instruments Ultra-High Frequency Quantum Analyzer (UHFQA) is an all-in-one two-channel AWG and two-channel digitizer which we use to perform readout. The AWG produces the envelopes of microwave readout pulses injected to a feedline. The digitizer performs demodulation and weighted integration of the feedline output signal (after amplification and frequency down-conversion) and thresholds, producing a one-bit outcome for each qubit measured. Starmon-5 makes use of two UHFQAs, one per feedline.

The QuTech Vector Switch Matrix (VSM) is 8-channel input, 32-channel output versatile analog instrument allowing custom conditioning and real-time routing of microwave pulses for single-qubit control. In Starmon-5, we only scratch the surface of the VSM capabilities: we simply use it as a bank of variable gain amplifiers. In the future, versions of the Starmon back-end with higher qubit count will take advantage of its advanced routing capabilities.

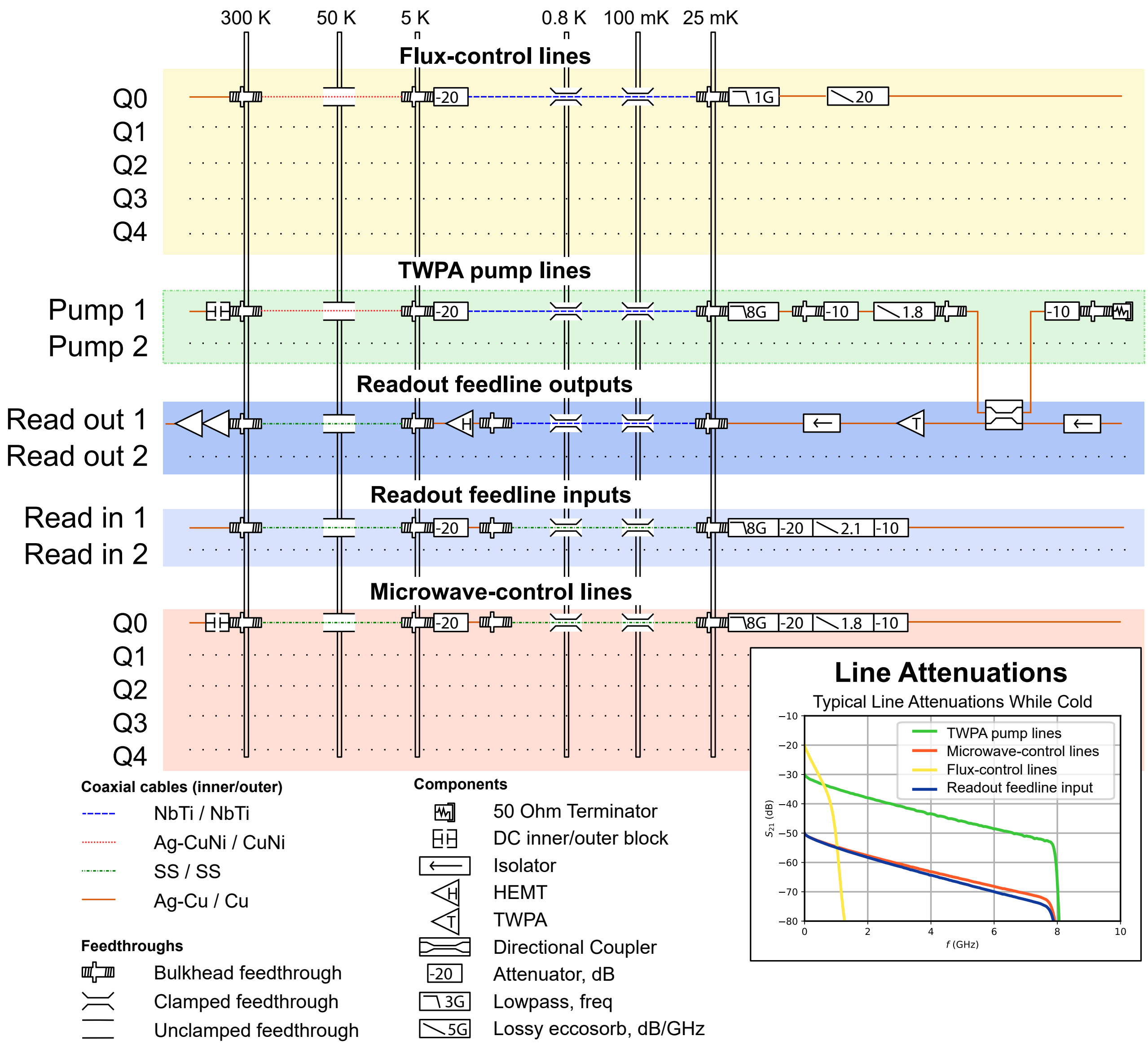

FIG. 3. Detailed fridge wiring diagram for Starmon-5.

IV. QUBIT OPERATIONS

Single-qubit gates: Native single-qubit gates are performed with microwave pulses resonant with the qubit transition frequency. We employ the standard DRAG pulse shape [7, 8] with its characteristic gaussian and derivative-of-gaussian envelopes. All single-qubit gates complete within 20 ns.

Two-qubit gates: The native two-qubit gate in Starmon-5 is the conditional-phase (CZ) gate. We realize this gate by exploiting the flux-controlled interaction between computational states $|11\rangle$ and the non-computational state $|02\rangle$, where 2 refers to the second excited state of one of the transmons in the pair [9]. We use the Net-Zero variant [10] of fast-adiabatic flux pulses [11]. All CZ gates in Starmon-5 complete within 60 ns (originally 80 ns, please see list of upgrades below).

Readout: Simultaneous, independent readout of the qubits is performed with a frequency-multiplexed pulsed measurement of feedline transmission at the frequencies of the readout-Purcell-filter pairs. Readout excitation pulses are 200 ns long. The response at each frequency is demodulated and integrated (with optimal weight functions [12]) over 800 ns.

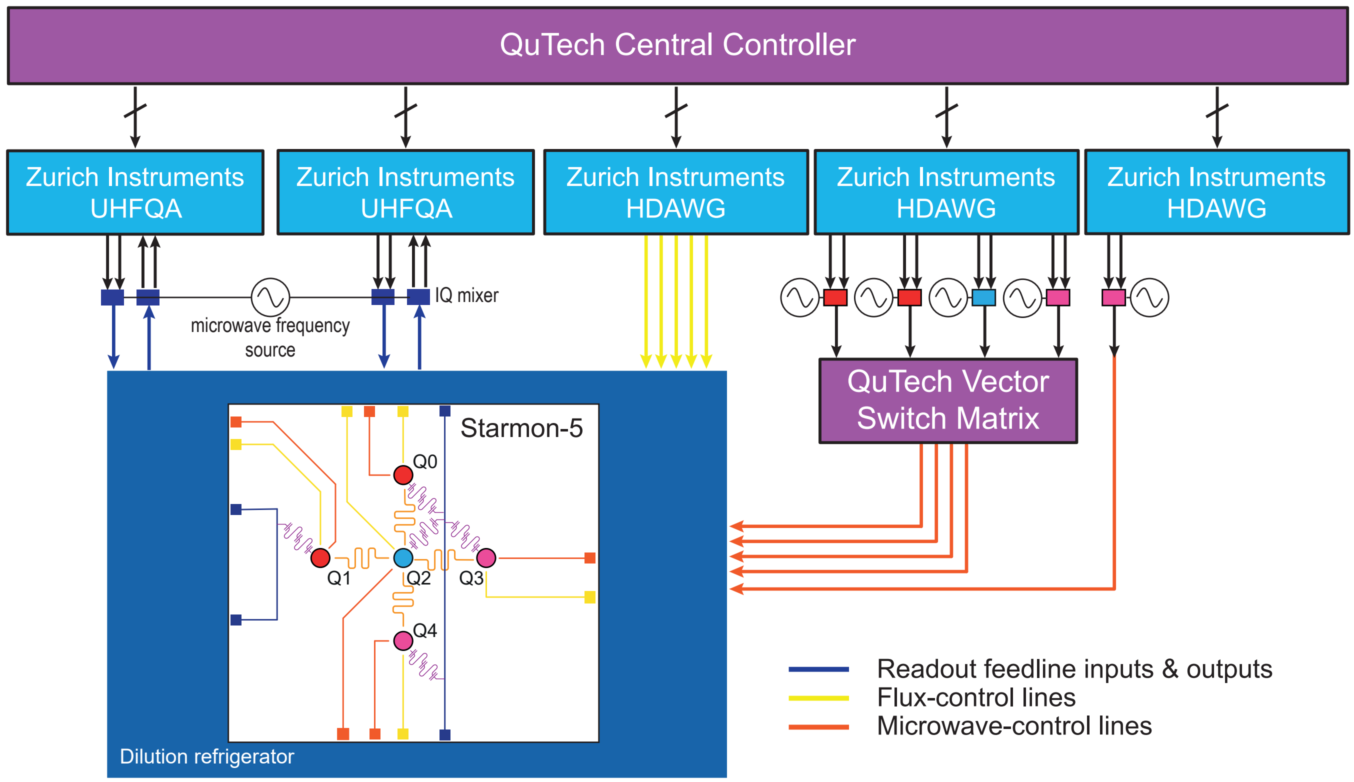

FIG. 4. Schematic diagram of the key instruments in the room-temperature electronics control stack of Starmon-5.

V. REPORTED METRICS

Qubit relaxation and dephasing times: The relaxation time T_1 and the dephasing time T_2^{echo} for each qubit are extracted from standard sliding-π pulse and Hahn-echo experiments, respectively [13].
Single-qubit gate fidelity $F_{1\mathrm{Q}}$: We perform single-qubit Clifford randomized benchmarking (RB) to extract an average error per single-qubit Clifford gate. Taking into account that 1.875 native gates are required on average per Clifford gate, we then extract the average error per native single-qubit gate [14].
Two-qubit gate fidelity $F_{2\mathrm{Q}}$: We perform two-qubit Clifford RB to extract an average error per two-qubit Clifford gate. Taking into account that 1.5 CZ gates are required on average per two-qubit Clifford gate, we then extract the average error per CZ gate assuming all error to arise from CZ gates [10].
Initialization fidelity F_{INIT}: We obtain a histogram [15] of the analog output of single-shot readout with the qubit initialized (ideally in $|0\rangle$). We perform a double-gaussian fit to this histogram and associate the dominant (weaker) gaussian to the analog readout for qubit in $|0\rangle$ ($|1\rangle$). The initialization fidelity is given by the ratio of the area of the dominant gaussian to the total area of the double gaussian.
Readout fidelity $F_{\mathrm{R/O}}$: We perform single-shot readout experiments to determine the probability $1-\epsilon_{10}$ of properly declaring measurement outcome 0 when the qubit is prepared in $|0\rangle$ and the probability $1-\epsilon_{01}$ of properly declaring 1 when prepared in $|1\rangle$, using the optimal 1-bit discretization threshold. We report the average assignment fidelity [16], given by $F_{\mathrm{R/O}} = 1 - (\epsilon_{10} + \epsilon_{01})/2$. The reported value corrects for the calibrated initialization error.

VI. STRUCTURE OF USER PROGRAMS

Use of prepare (measure) commands should be restricted to a single line in the beginning (end) of a program. To allow for the initialization (measurement) in different bases for different qubits, the cQASM parellel construct must be used to group statements. For example, the initialization of qubits Q_0 and Q_3 in the X basis, Q_1 and Q_2 in the Y basis, and Q_4 in the Z basis is specified as follows:

$$\{prep\_x\ q[0,3] \mid prep\_y\ q[1,2] \mid prep\_z\ q[4]\}.$$

Any unspecified qubits will be initialized in the Z basis. The measurement of qubits Q_0 and Q_4 in the X basis, Q_1 and Q_3 in the Y basis, and Q_2 in the Z basis is specified as follows:

$$\{meas\_x\ q[0,4] \mid meas\_y\ q[1,3] \mid meas\_z\ q[2]\}.$$

VII. LIST OF MAJOR CHANGES AND UPGRADES

April 27, 2020: Added support for generalized initialization and measurement operations.

May 13, 2020: Shortened the duration of the four native two-qubit CZ gates from 80 to 60 ns.

May 18, 2020: Added initialization by post-selection to improve initialization fidelities. This post-selection happens behind the scenes and performs sufficient shots to ensure that the user gets back the number of shots they requested.

May 25, 2020: Increased the maximum possible number of shots per job to 16384.

June 1, 2020: Improved readout calibration to increase average readout fidelity above 97%.

June 8, 2020: Added support for arbitrary single-qubit rotations around the X, Y, and Z axes of the Bloch sphere. Rotations angles are quantized to the nearest multiple of $\pi \times 2^{-5}$.

VIII. REQUESTS FOR ADDITIONAL MATERIALS

For additional technical information regarding the Starmon-5 quantum chip, fridge wiring, control electronics, and reported metrics, please contact Miguel Moreira (miguel.moreira@tudelft.nl) or Leonardo DiCarlo (l.dicarlo@tudelft.nl).

ACKNOWLEDGMENTS

We thank W. Oliver and G. Calusine for providing the superconducting parametric amplifiers at the front end of each readout amplification chain.

[1] A. Blais, R.-S. Huang, A. Wallraff, S. M. Girvin, and R. J. Schoelkopf, Phys. Rev. A **69**, 062320 (2004).
[2] A. Wallraff, D. I. Schuster, A. Blais, L. Frunzio, R.-S. Huang, J. Majer, S. Kumar, S. M. Girvin, and R. J. Schoelkopf, Nature **431**, 162 (2004).
[3] J. A. Schreier, A. A. Houck, J. Koch, D. I. Schuster, B. R. Johnson, J. M. Chow, J. M. Gambetta, J. Majer, L. Frunzio, M. H. Devoret, S. M. Girvin, and R. J. Schoelkopf, Phys. Rev. B **77**, 180502 (2008).
[4] J. Heinsoo, C. K. Andersen, A. Remm, S. Krinner, T. Walter, Y. Salathé, S. Gasparinetti, J.-C. Besse, A. Potočnik, A. Wallraff, and C. Eichler, Phys. Rev. Appl. **10**, 034040 (2018).
[5] R. Versluis, S. Poletto, N. Khammassi, B. M. Tarasinski, N. Haider, D. J. Michalak, A. Bruno, K. Bertels, and L. DiCarlo, Phys. Rev. Appl. **8**, 034021 (2017).
[6] M. A. Rol, L. Ciorciaro, F. K. Malinowski, B. M. Tarasinski, R. E. Sagastizabal, C. C. Bultink, Y. Salathe, N. Haandbaek, J. Sedivy, and L. DiCarlo, Applied Physics Letters **116**, 054001 (2020).
[7] F. Motzoi, J. M. Gambetta, P. Rebentrost, and F. K. Wilhelm, Phys. Rev. Lett. **103**, 110501 (2009).
[8] J. M. Chow, L. DiCarlo, J. M. Gambetta, F. Motzoi, L. Frunzio, S. M. Girvin, and R. J. Schoelkopf, Phys. Rev. A **82**, 040305 (2010).

[9] L. DiCarlo, J. M. Chow, J. M. Gambetta, L. S. Bishop, B. R. Johnson, D. I. Schuster, J. Majer, A. Blais, L. Frunzio, S. M. Girvin, and R. J. Schoelkopf, Nature **460**, 240 (2009).

[10] M. A. Rol, F. Battistel, F. K. Malinowski, C. C. Bultink, B. M. Tarasinski, R. Vollmer, N. Haider, N. Muthusubramanian, A. Bruno, B. M. Terhal, and L. DiCarlo, Phys. Rev. Lett. **123**, 120502 (2019).

[11] J. M. Martinis and M. R. Geller, Phys. Rev. A **90**, 022307 (2014).

[12] C. C. Bultink, B. Tarasinski, N. Haandbaek, S. Poletto, N. Haider, D. J. Michalak, A. Bruno, and L. DiCarlo, Appl. Phys. Lett. **112**, 092601 (2018).

[13] P. Krantz, M. Kjaergaard, F. Yan, T. P. Orlando, S. Gustavsson, and W. D. Oliver, Appl. Phys. Rev. **6**, 021318 (2019).

[14] M. A. Rol, C. C. Bultink, T. E. O'Brien, S. R. de Jong, L. S. Theis, X. Fu, F. Luthi, R. F. L. Vermeulen, J. C. de Sterke, A. Bruno, D. Deurloo, R. N. Schouten, F. K. Wilhelm, and L. DiCarlo, Phys. Rev. Applied **7**, 041001 (2017).

[15] D. Ristè, J. G. van Leeuwen, H.-S. Ku, K. W. Lehnert, and L. DiCarlo, Phys. Rev. Lett. **109**, 050507 (2012).

[16] C. C. Bultink, M. A. Rol, T. E. O'Brien, X. Fu, B. C. S. Dikken, C. Dickel, R. F. L. Vermeulen, J. C. de Sterke, A. Bruno, R. N. Schouten, and L. DiCarlo, Phys. Rev. Appl. **6**, 034008 (2016).